Atmospheric
Chemistry
and Physics

Supplement of

Measurement report: Optical and structural properties of atmospheric water-soluble organic carbon in China – insights from multi-site spectroscopic measurements

Haibiao Chen et al.

Correspondence to: Caiqing Yan (cyan0325@sdu.edu.cn)

Text S1. Determination of primary and secondary organic carbon.

The concentrations of primary organic carbon (POC) and secondary organic carbon (SOC) are estimated by the EC tracer method as follows,

$$SOC = OC - EC \times (OC/EC)_{min} \tag{S1}$$

$$POC = OC - SOC \tag{S2}$$

where $(OC/EC)_{min}$ is the minimum OC/EC ratio during the sampling period at each site.

Text S2. Calculation of light absorption parameters.

The light absorption coefficient (Abs_λ, Mm^{-1}) of WSOC at the wavelength λ is calculated as follows,

$$Abs_\lambda = (A_\lambda - A_{700}) \times \frac{V_l}{V_a \times L} \times \ln(10) \tag{S3}$$

where V_l (mL) is the volume of the water extracts, V_a (m^3) is the air volume corresponding to the extracted sample filter, and L is the optical path length (1 m in this study). A_λ is the absorbance at wavelength λ measured by the spectrophotometer. A_{700} is chosen to reduce the effects of baseline drift and $\ln(10)$ is used to convert the absorption coefficient from log base 10 to natural logarithm. In this study, Abs_{365} is chosen as a proxy for the absorbance of WSOC to exclude the interferences of other substances (e.g., nitrate, etc.) (Hecobian et al., 2010).

The mass absorption efficiency (MAE, $m^2 \cdot g^{-1}$) of WSOC is calculated as follows,

$$MAE_\lambda = \frac{Abs_\lambda}{C_{WSOC}} \tag{S4}$$

where C_{WSOC} ($\mu g \cdot m^{-3}$) represents the mass concentration of WSOC.

The wavelength dependence of light absorption fits a power law as follows,

$$Abs_\lambda = K \times \lambda^{-AAE} \tag{S5}$$

where K is a constant related to light absorption and AAE is the absorption Ångström exponent used to characterize the wavelength dependence of WSOC light absorption. In this study, AAE is fitted over the wavelength range of 300-500 nm in consideration of avoiding the interference from light-absorbing inorganic compounds (e.g., ammonium nitrate, sodium nitrate and nitrate ions) at shorter wavelengths (< 250 nm) and ensuring significant light absorption signals of WSOC at longer wavelengths (Afsana et al., 2022; Ting et al., 2022; Yan et al., 2015). Moreover, the power-law fit of all samples' absorption coefficients between 300 and 500 nm is good with $r^2 > 0.99$ (see Figure S2).

The imaginary part (k) of the particle refractive index ($m = n + ik$) is an important parameter that evaluates the light-absorbing efficiency of aerosols. In this study, we calculate the k_{405} based on equation S6 and use $\log_{10}(MAE_{405})$ vs. AAE to classify different light-absorbing BrC (Saleh, 2020). To unify and facilitate comparison, the MAE_{365} values reported in previous studies are converted to MAE_{405} by the following equations (Liu et al., 2013; Saleh, 2020),

$$k_\lambda = \frac{MAE_\lambda \times \lambda \times \rho}{4\pi} \tag{S6}$$

$$k_{365} = k_{\lambda} \left(\frac{\lambda}{365} \right)^{w} \tag{S7}$$

$$w = \text{AAE} - 1 \tag{S8}$$

where ρ is particle density and assign as 1.5 g·cm^{-3} in this study.

Text S3. Estimation of direct radiative effect of water-soluble organic carbon.

60   Simple forcing efficiency (SFE) represents the energy added to the Earth-atmosphere system by a given mass of particles (Bond and Bergstrom, 2006). In this study, dSFE(λ)/$d\lambda$ (W·m^{-2}·nm^{-1}) and integrated SFE (W·g^{-1}) over the wavelength ranges of 300-400 nm and 300-700 nm are calculated by following equations (S9 and S10) to estimate the direct radiative forcing of WSOC (Chen and Bond, 2010),

$$\frac{d\text{SFE}}{d\lambda} = -\frac{1}{4} \frac{d\text{S}(\lambda)}{d\lambda} \, \tau_{\text{atm}}^{2}(\lambda) \, (1 - F_{c}) \left[2(1 - \alpha_{s})^{2} \, \beta(\lambda) \, \text{MSE}(\lambda) - 4\alpha_{s} \, \text{MAE}(\lambda) \right] \tag{S9}$$

65
$$\text{SFE} = \int_{\lambda} \frac{d\text{S}(\lambda)}{d\lambda} \, \tau_{\text{atm}}^{2}(\lambda) \, (1 - F_{c}) \, \alpha_{s} \, \text{MAE}(\lambda) \, d\lambda \tag{S10}$$

where $d\text{S}(\lambda)/d\lambda$ is the solar irradiance (W·m^{-2}·nm^{-1}) obtained from the ASTM G173-03 reference spectra, τ_{atm} is the atmospheric transmission (0.79), F_{c} is the cloud fraction (0.6), α_{s} is the surface albedo (average 0.19), β is the backscatter fraction, MSE and MAE are the mass scattering efficiency and mass absorption efficiency of WSOC, respectively. It should be noted that $\beta = 0$ and only light absorption is considered in the calculation in this study.

70   **Text S4. Light absorption spectra resolved by positive matrix factorization (PMF) model.**

The positive matrix factorization (PMF) model is performed on the light absorption spectra of WSOC using the EPA PMF model (version 5.0). The rationale and detailed descriptions can be found in the PMF 5.0 Fundamentals and User Guide on the EPA website (https://www.epa.gov/air-research/epa-positive-matrix-factorization-50-fundamentals-and-user-guide). In this study, absorbance data in the wavelength range of 250 to 500 nm (interval 5 nm) and corresponding uncertainties are included

75   in the PMF analysis. The absorbance data below the method detection limit (MDL, 1.0 mAu in this study) are replaced by 1/2 MDL (Li et al., 2023b). The uncertainty (Unc) is calculated according to the following equations when the absorbance $\leq$ MDL (equation S11) and the absorbance > MDL (equation S12), respectively,

$$\text{Unc} = 5/6 \, \text{MDL} \tag{S11}$$

$$\text{Unc} = \sqrt{(\text{Error Fraction} \times \text{absorbance})^{2} + (0.5 \times \text{MDL})^{2}} \tag{S12}$$

80   where the error fraction is set as 0.2 in this study.

In this study, the WSOC absorption spectra of the ten sites can be roughly divided into two categories: (1) unimodal, that is, the light absorption continues to decline from 250 nm to 700 nm, with a peak around 250 nm; (2) bimodal, that is, there are two significant absorption peaks at 265 nm and 300 nm (see Figure 4). Interestingly, these two types of spectra happen to correspond to the east China sites (i.e., QD, NJ, SH and TS) and the outside east China sites (i.e., TJ, HD, XA, CD, CQ and

85   HS), respectively. Therefore, the WSOC spectra of the two categories were separately put into the PMF model for analysis. In view of the fact that WSOCs at ten sites all have relatively significant light absorption in the range of 250-500 nm, and in order to be consistent with the calculation range of AAE, PMF analysis is carried out for spectra in the band range of 250-500 nm.

Text S5. PARAFAC analysis and calculation of fluorescence parameters.

All the excitation emission matrices (EEMs) data are normalized by the water Raman peak area (Ex = 350 nm, Em = 385-410
90   nm) and the data are ultimately presented in Raman units (RU) (Lawaetz and Stedmon, 2009). Parallel factor analysis (PARAFAC) with the non-negativity constraint of Raman normalized EEMs data is performed using the DOMFluor toolbox (v 1.7) in MATLAB R2020a to identify the potential fluorophores (Stedmon and Bro, 2008). Besides, fluorescent indices are calculated to provide source and structure information of atmospheric organic aerosols. The fluorescence index (FI), biological index (BIX) and humidification index (HIX) are determined according to the following equations (Wu et al., 2021),
95   respectively.

$$FI = \frac{F(E_x = 370 \text{ nm}, E_m = 450 \text{ nm})}{F(E_x = 370 \text{ nm}, E_m = 500 \text{ nm})} \tag{S13}$$

$$BIX = \frac{F(E_x = 310 \text{ nm}, E_m = 380 \text{ nm})}{F(E_x = 310 \text{ nm}, E_m = 430 \text{ nm})} \tag{S14}$$

$$HIX = \frac{F(E_x = 255 \text{ nm}, E_m = 435\text{-}480 \text{ nm})}{F(E_x = 255 \text{ nm}, E_m = 300\text{-}345 \text{ nm})} \tag{S15}$$

It should be noted that FI (BIX) refers to the ratio of emission intensity of 450 and 500 nm (380 and 430 nm) at Ex = 370 nm
100   (310 nm), while HIX is calculated with the integrated intensity over the wavelength range of 435-480 nm and 300-345 nm at Ex = 255 nm. In this study, these fluorescent indices are calculated by the EFC software (v 1.2) (Bro, 1997; He and Hur, 2015; Murphy et al., 2010; Stedmon and Bro, 2008; Zepp et al., 2004).

Moreover, the total fluorescence volume (TFV; RU-nm^2) and fluorescence volume (FV; RU-nm^2) of each fluorophore are calculated by integrating the Raman normalized EEMs data in MATLAB R2020a.

105   **Text S6. Methods for extreme gradient boosting (XGBoost).**

The extreme gradient boosting (XGBoost) model is a gradient-boosting-based ensemble algorithm that improves traditional techniques with remarkable attributes, including efficiency, precision, stability, and scalability (Li et al., 2024). In this study, XGBoost is used to evaluate the contribution of conventional air pollutants (e.g., CO, SO$_2$, O$_3$, NO$_2$) and fluorescent components to the light absorption coefficient (Abs$_{365}$). The national air quality data comes from the real-time release platform
110   of the China Environmental Monitoring Station for urban air quality nationwide (https://quotsoft.net/air/). To further quantify the contributions of the target factors, the SHAP algorithm is introduced, which evaluates the feature contributions based on the marginal contributions of individuals in cooperative games (Li et al., 2024). The main formulas are as follows,

$$f(x) = \varphi_0(f,x) + \sum_{i=1}^{k} \varphi_i(f,x) \tag{S16}$$

$$\varphi_i(f,x) = \sum_{S \subseteq F \setminus \{i\}} \frac{|S|!(k-|S|-1)!}{k!} (f_x(S \cup \{i\}) - f_x(S)) \tag{S17}$$

115 where $\varphi_0(f, x)$ denotes the expected value of the light absorption coefficient predicted by the model on the training set. k is the number of factors influencing the model. $\varphi_i(f, x)$ can be interpreted as the impact of the i-th factor on the prediction of the model when given an input x.

All operations are performed in Python 3.10 using Jupyter as an integrated coding environment. The following Python packages are used in this study: *scikit-learn* provides a standard interface for implementing machine learning algorithms,

120 *pandas* and *NumPy* for data analysis process, *BayesSearchCV* for parameter optimization, *matplotlib* for data visualization, and *SHAP* for result interpretation (Li et al., 2024).

Table S1. Summary of the sampling information.

Sites	Location	Region	Sampling period	Sample size	Sampling duration	Sampler	Filter
Tianjin (TJ)	39.11°N, 117.19°E	north China	2019/11/29 to 2020/01/06	41	23.5 h	medium-volume (100 L min^{-1}) sampler (TH-150A, Wuhan Tianhong, China)	QMA, Φ90 mm, (Whatman, USA)
Handan (HD)	36.57°N, 114.50°E		2019/12/26 to 2020/01/01	16	11.5 h	medium-volume (100 L min^{-1}) sampler (TH-150A, Wuhan Tianhong, China)	QMA, Φ90 mm, (Whatman, USA)
Qingdao (QD)	36.35°N, 120.67°E	east China	2019/11/11 to 2019/12/27	46	23.5 h	medium-volume (100 L min^{-1}) sampler (TH-150A, Wuhan Tianhong, China)	QMA, Φ90 mm, (Whatman, USA)
Nanjing (NJ)	32.21°N, 118.71°E		2019/12/02 to 2019/12/31	51	11 h	high-volume (300 L min^{-1}) sampler (ASM-1, Guangzhou Mingye, China)	QMA, 8×10 in, (Munktell, SE)
Shanghai (SH)	31.17°N, 121.44°E		2020/12/01 to 2020/12/28	20	22 h	high-volume (1.13 m^3 min^{-1}) sampler (Tisch Environment, USA)	QMA, 8×10 in, (Whatman, USA)
Xi'an (XA)	34.38°N, 108.98°E	northwest China	2019/11/21 to 2019/12/20	30	23.5 h	high-volume (1 m^3 min^{-1}) sampler (XT-1025, Shanghai Xintuo, China)	QMA, 8×10 in, (Whatman, USA)
Chengdu (CD)	30.58°N, 103.99°E	southwest China	2019/11/23 to 2020/01/04	37	23.5 h	medium-volume (100 L min^{-1}) sampler (TH-150A, Wuhan Tianhong, China)	QMA, Φ90 mm, (Whatman, USA)
Chongqing (CQ)	29.56°N, 106.45°E		2019//12/24 to 2020/01/08	17	23.5 h	high-volume (300 L min^{-1}) sampler (ASM-1, Guangzhou Mingye, China)	QMA, 8×10 in, (Whatman, USA)
Mt. Tai (TS)	36.25°N, 117.10°E	regional site	2019/12/05 to 2020/01/02	49	11.5 h	medium-volume (60 L min^{-1}) sampler (LY-2030, Qingdao Laoying, China)	QMA, Φ90 mm, (Whatman, USA)
Heshan (HS)	22.74°N, 112.95°E		2019/11/11 to 2020/01/21	15	24 h	high-volume (1 m^3 min^{-1}) sampler (XT-1025, Shanghai Xintuo, China)	QMA, 8×10 in, (Whatman, USA)

Table S2. Mass concentrations and related ratios of carbonaceous components measured in this study.

Sites	Regions	OC (µg·m⁻³) Avg ± SD	EC (µg·m⁻³) Avg ± SD	WSOC (µg·m⁻³) Avg ± SD	OC/EC Avg ± SD	WSOC/OC (%) Avg ± SD	POC (µg·m⁻³) Avg ± SD	SOC (µg·m⁻³) Avg ± SD
Tianjin (TJ)	north China	10.0 ± 6.06	1.20 ± 0.53	5.96 ± 3.21	7.99 ± 2.08	59.9 ± 11.8	5.64 ± 2.47	4.38 ± 3.94
Handan (HD)		17.9 ± 8.56	2.44 ± 0.48	10.6 ± 5.33	7.06 ± 2.52	55.2 ± 13.3	8.79 ± 1.72	9.08 ± 7.34
Qingdao (QD)	east China	8.69 ± 5.60	1.34 ± 0.83	4.68 ± 3.01	6.45 ± 1.15	55.1 ± 11.6	5.86 ± 3.62	2.83 ± 2.49
Nanjing (NJ)		10.6 ± 4.16	2.36 ± 0.83	6.82 ± 2.00	4.58 ± 0.93	65.2 ± 11.9	7.03 ± 2.48	3.61 ± 2.84
Shanghai (SH)		3.31 ± 1.48	0.35 ± 0.16	1.97 ± 0.83	10.1 ± 2.69	61.0 ± 6.99	1.72 ± 0.79	1.59 ± 0.94
Xi'an (XA)	northwest China	17.8 ± 7.24	2.86 ± 1.49	10.2 ± 4.55	6.90 ± 1.65	57.3 ± 6.93	12.9 ± 6.74	4.87 ± 2.37
Chengdu (CD)	southwest China	12.2 ± 4.48	1.87 ± 0.51	8.98 ± 3.09	6.44 ± 1.41	73.3 ± 10.0	6.02 ± 1.63	6.17 ± 3.22
Chongqing (CQ)		19.6 ± 6.48	2.25 ± 0.79	10.5 ± 3.45	9.02 ± 1.94	53.4 ± 4.94	13.6 ± 4.78	5.96 ± 3.98
Mt. Tai (TS)	regional site	4.17 ± 2.73	0.71 ± 0.74	3.60 ± 1.22	6.97 ± 3.11	65.1 ± 19.6	1.91 ± 2.00	2.26 ± 1.58
Heshan (HS)		9.17 ± 3.54	1.38 ± 0.31	5.85 ± 2.12	6.45 ± 1.52	64.4 ± 11.9	5.37 ± 1.20	3.80 ± 2.55

125
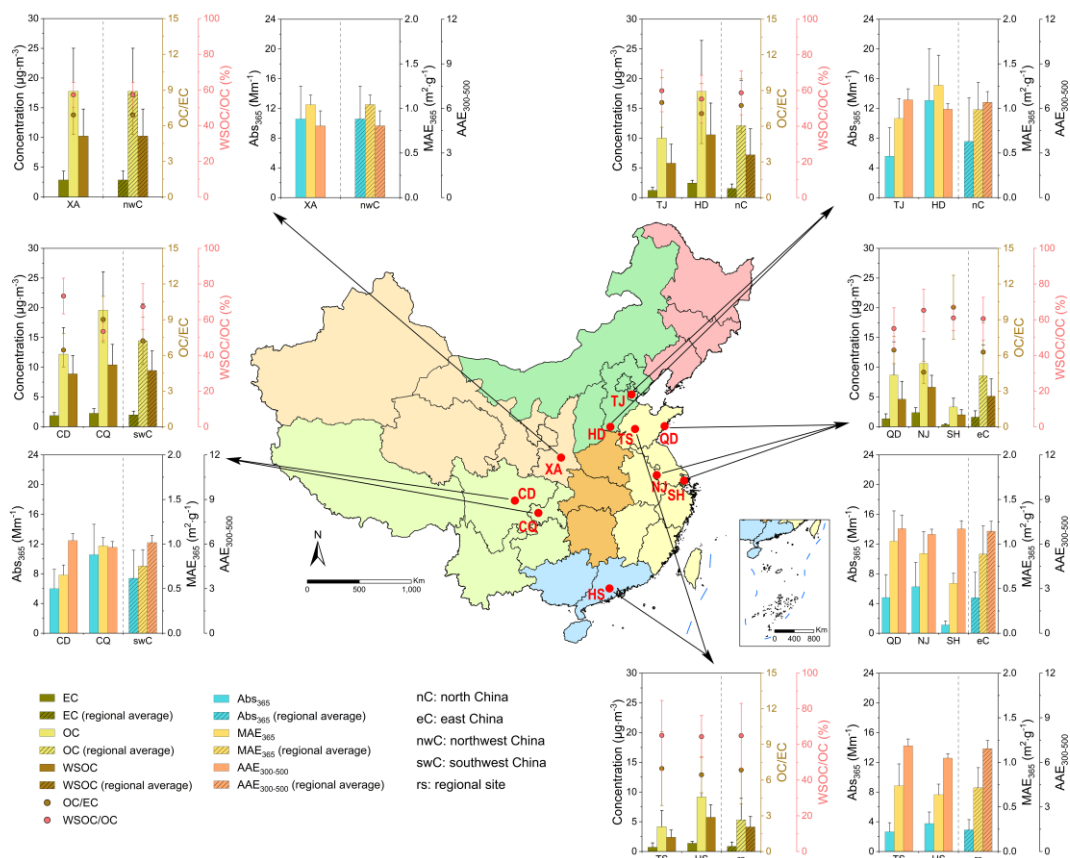
Figure S1. Location map of ten sampling sites and mass concentrations of carbonaceous components (OC, EC and WSOC), OC/EC and WSOC/OC ratios, and light absorption coefficients and mass absorption efficiencies at 365 nm, as well as absorption Ångström exponent at 300-500 nm of WSOC at each site. Note: Data used in the figure are all average values, with shaded columns representing the average value of each region (nwC: northwest China; nC: north China; swC: southwest China; eC: east China; and rs: regional sites) where the sampling sites locate. The administration boundaries in the map are originated from the Resource and Environmental Science Data Platform (http://www.resdc.cn/ DOI,2023.DOI:10.12078/2023010103). © Institute of Geographic Sciences and Natural Resources Research, Chinese Academy of sciences.
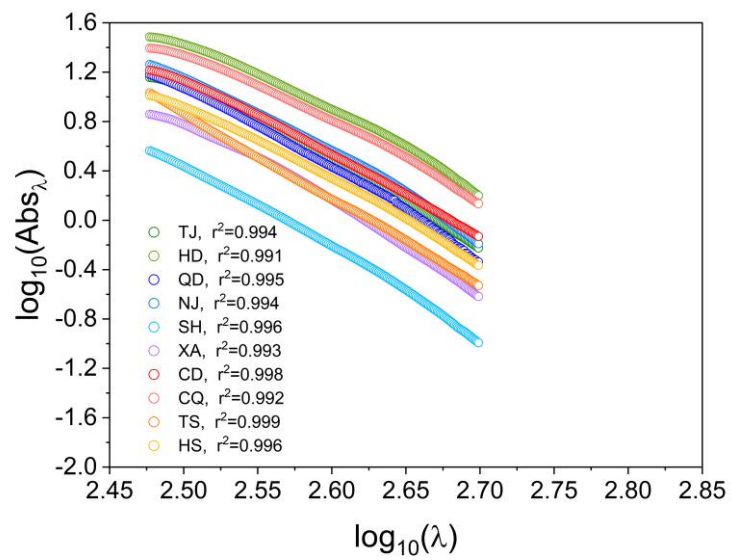
Figure S2. The power-law fitting curves of light absorption in the wavelength range of 300-500 nm.
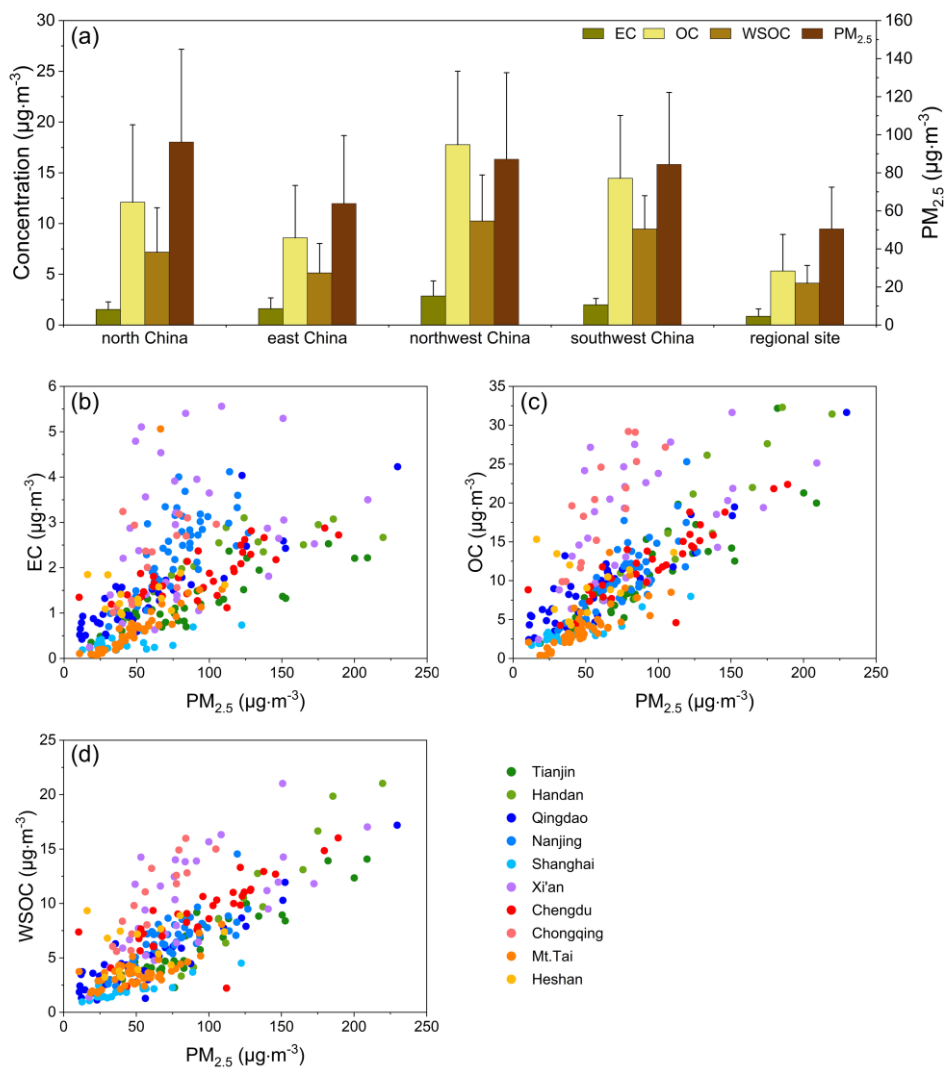
135

Figure S3. (a) Regional average carbonaceous component and PM$_{2.5}$ concentrations, and scatter plots of (b) EC, (c) OC and (d) WSOC with PM$_{2.5}$.
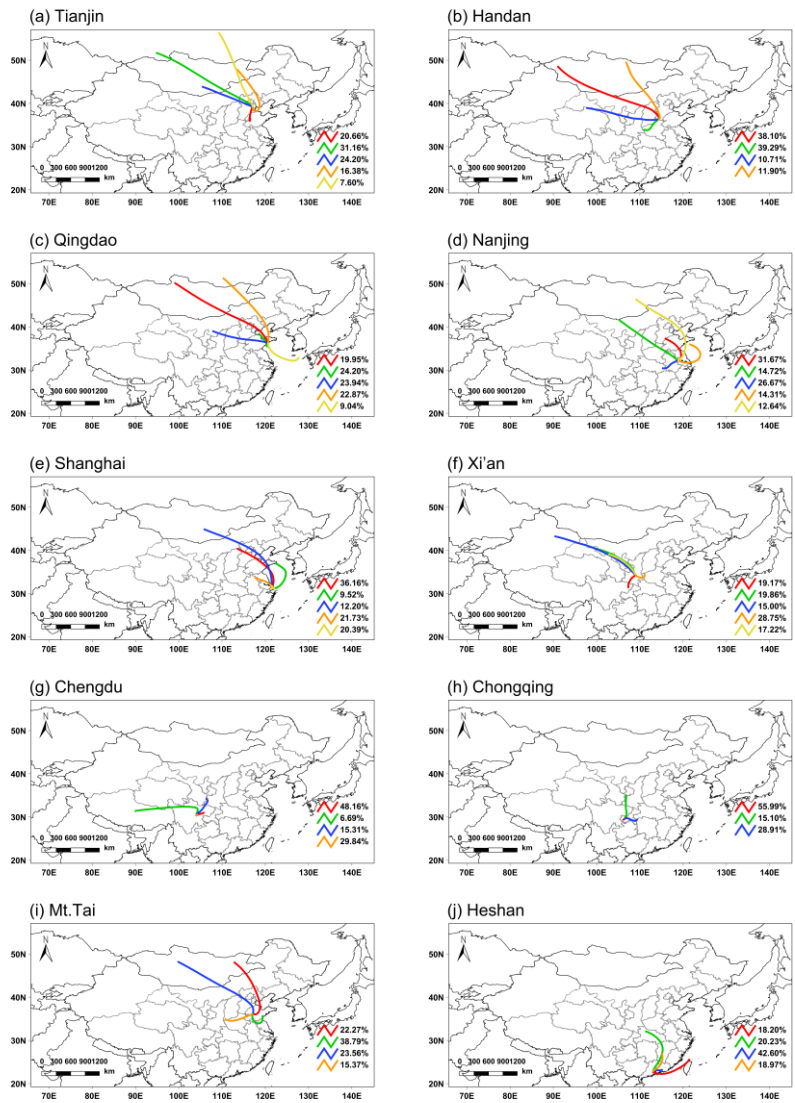
Figure S4. Clusters of air masses derived from backward trajectory analysis at the ten sites. The 48-h backward trajectories at each site are calculated every 1 h and clustered at an ending height of 500 m above ground level based on the MeteoInfoMap software.
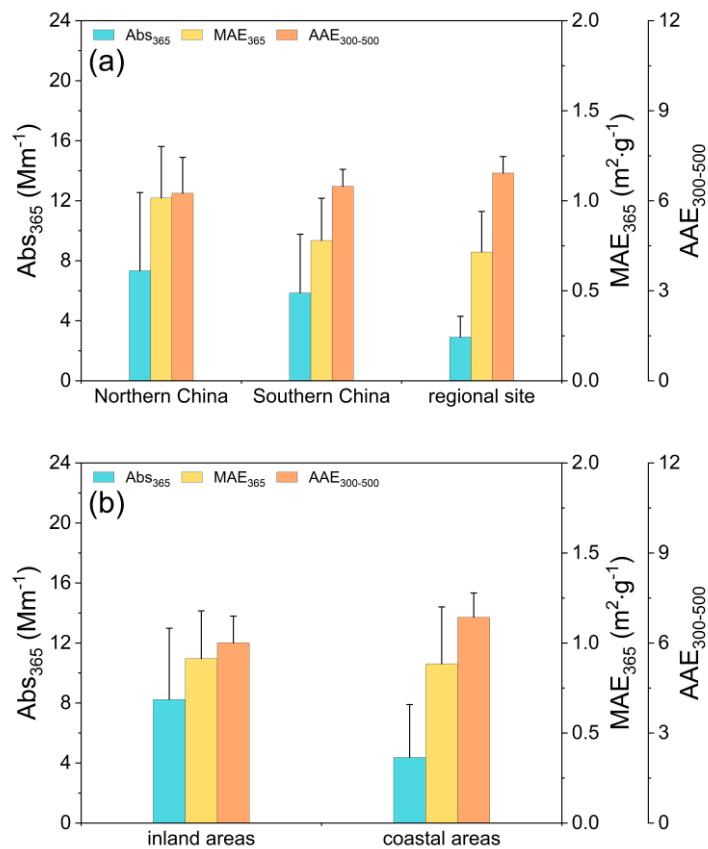
Figure S5. The average values of light absorption parameters (Abs_{365}, MAE_{365} and $AAE_{300-500}$) in (a) Northern and Southern China, (b) inland and coastal areas.
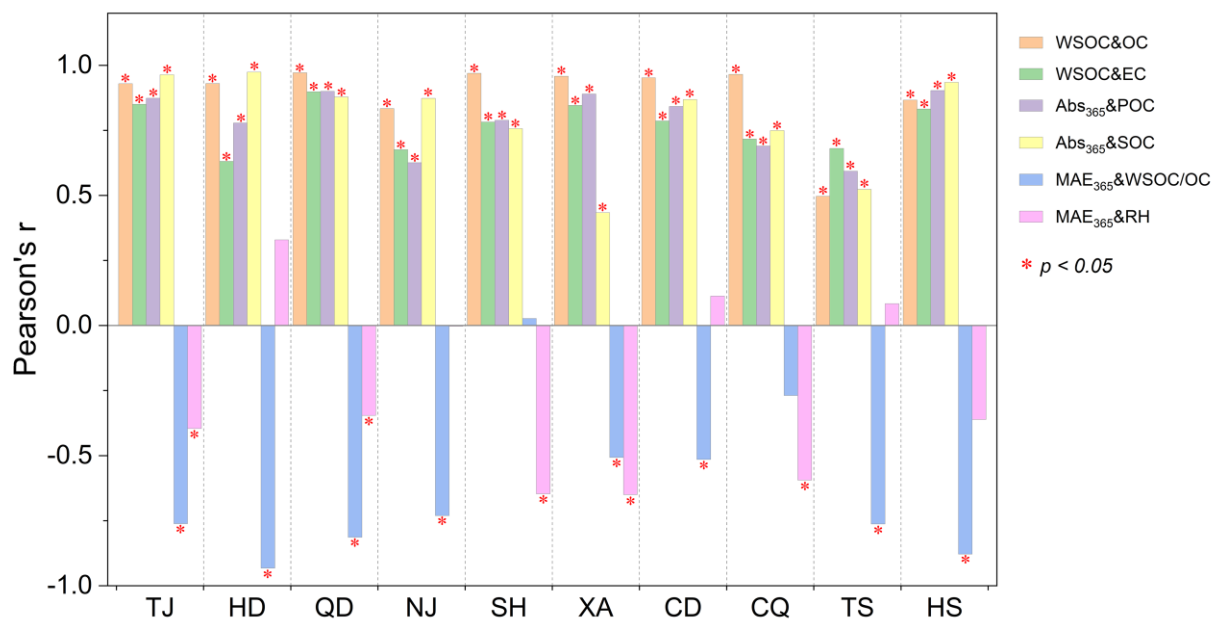
145

Figure S6. Pearson's correlation coefficients and significance levels (*p*, two-tailed) among different carbonaceous components (e.g., OC, EC, POC, SOC, WSOC/OC), light-absorbing parameters (e.g., MAE_{365}, Abs_{365}) and RH at each site.
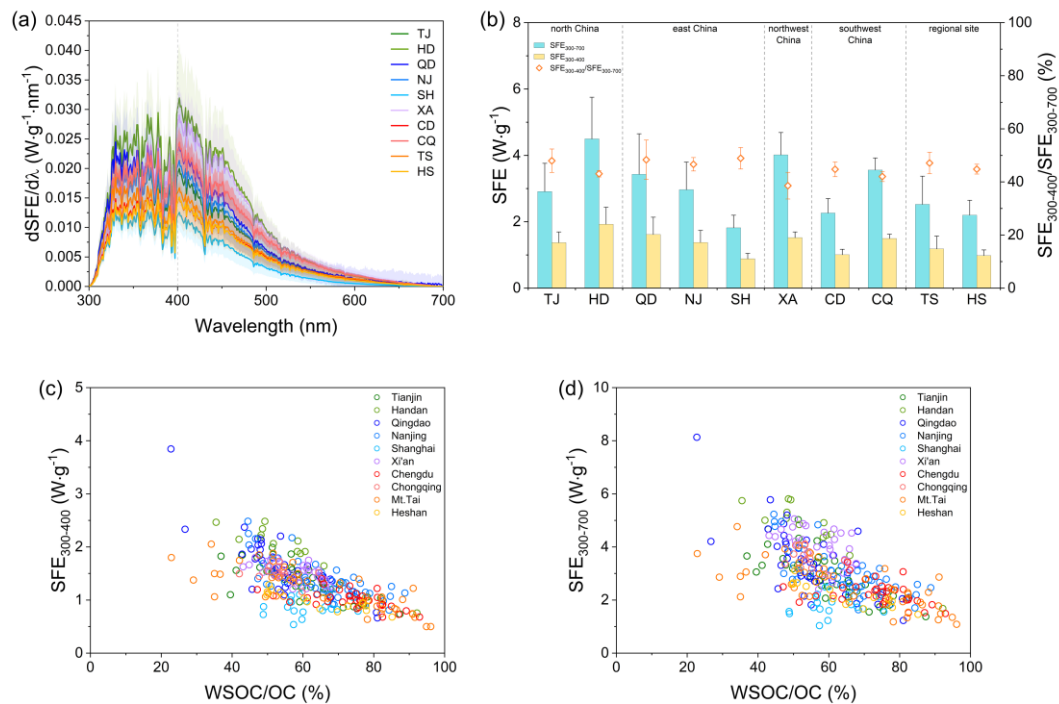
Figure S7. (a) SFE spectra of WSOC at different sites, (b) the integrated SFE values over the wavelength of 300-400 nm and 300-700 nm, (c) and (d) the scatter plots of the relationship between $SFE_{300-400}$ ($SFE_{300-700}$) and WSOC/OC.
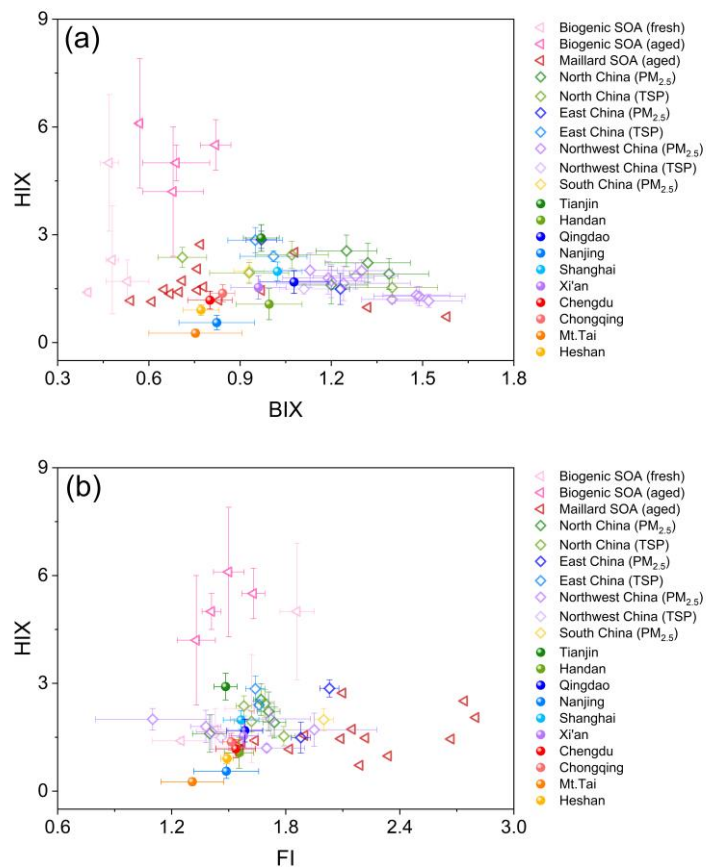
Figure S8. Scatter plots of HIX versus (a) BIX and (b) FI for WSOC measured in this study and reported in literatures (Deng et al., 2022; Fan et al., 2023; Gao et al., 2021; Lee et al., 2013; Li et al., 2023a; Li et al., 2023c; Qin et al., 2018; Wen et al., 2021; Xie et al., 2020; Yu et al., 2023; Zhan et al., 2022; Zhang et al., 2021; Zhong et al., 2023).
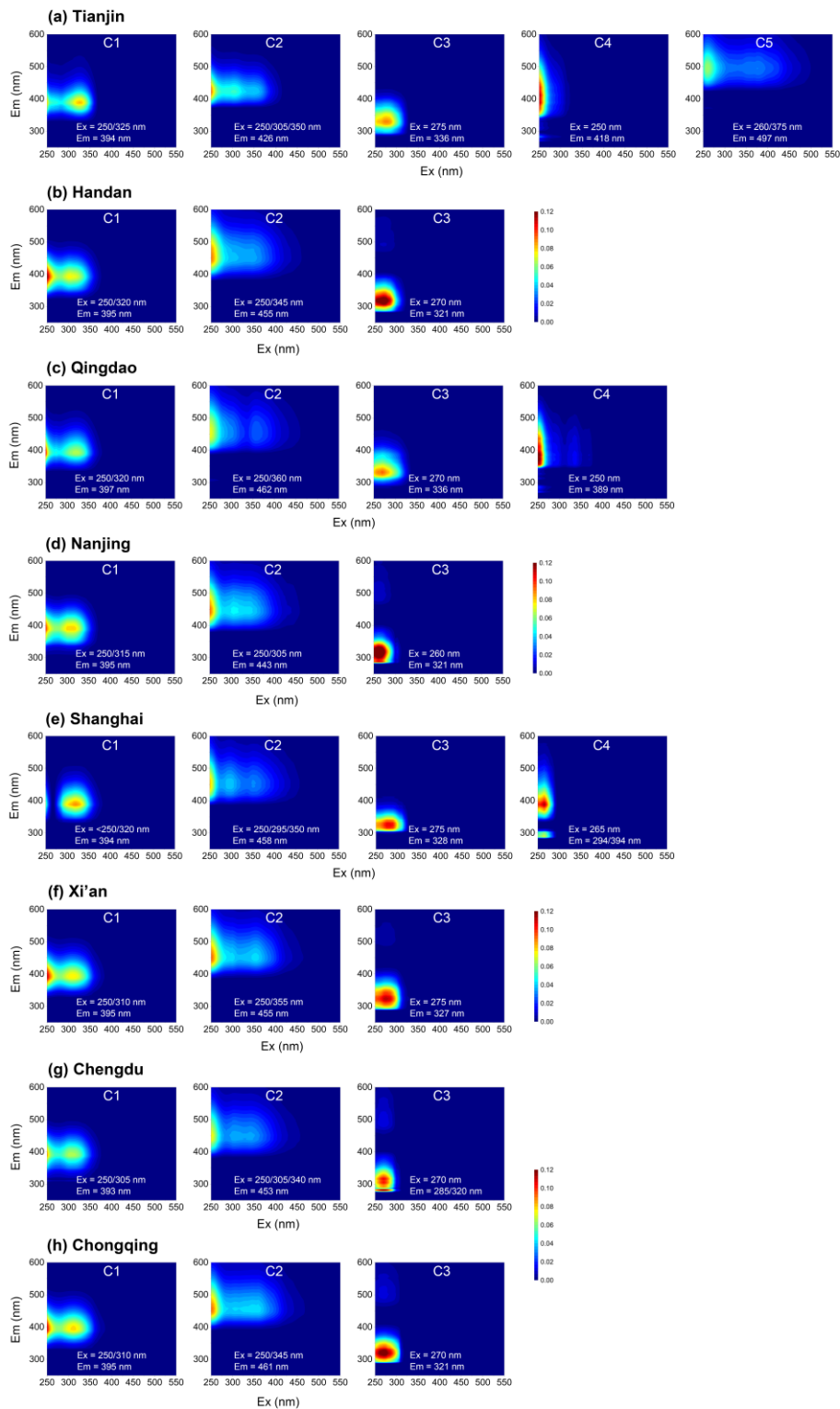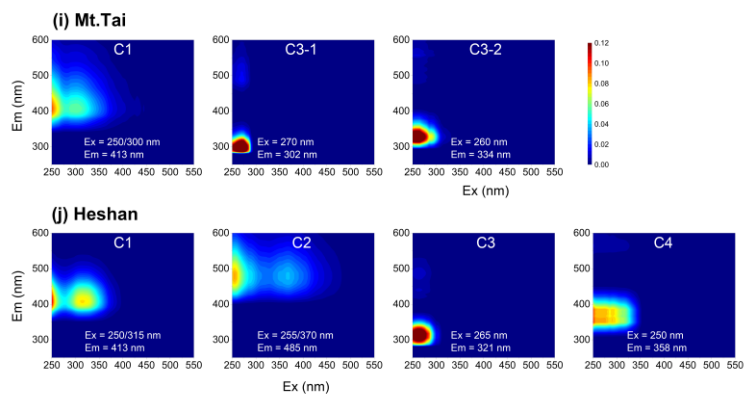
Figure S9. Contour plots of the fluorophores identified by PARAFAC analysis in (a) Tianjin, (b) Handan, (c) Qingdao, (d) Nanjing, (e) Shanghai, (f) Xi'an, (g) Chengdu, (h) Chongqing, (i) Mt. Tai and (j) Heshan.
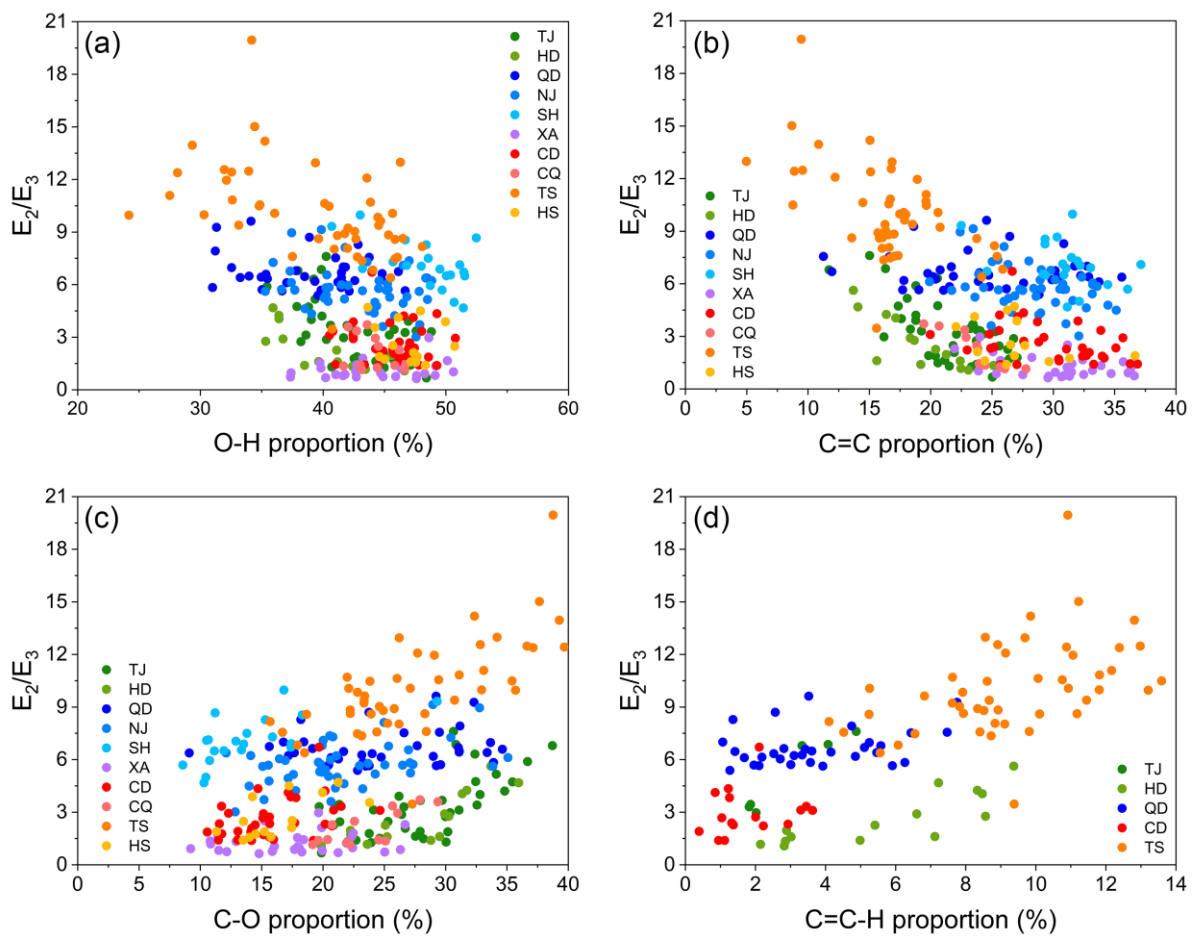
160   **Figure S10.** Scatter plots of the relative proportion of different functional groups (a) O-H, (b) C=C, (c) C-O and (d) C=C-H

with E_2/E_3 value at each site.
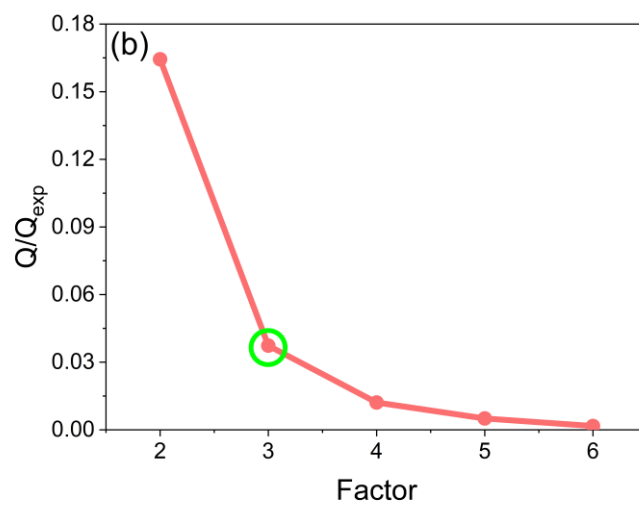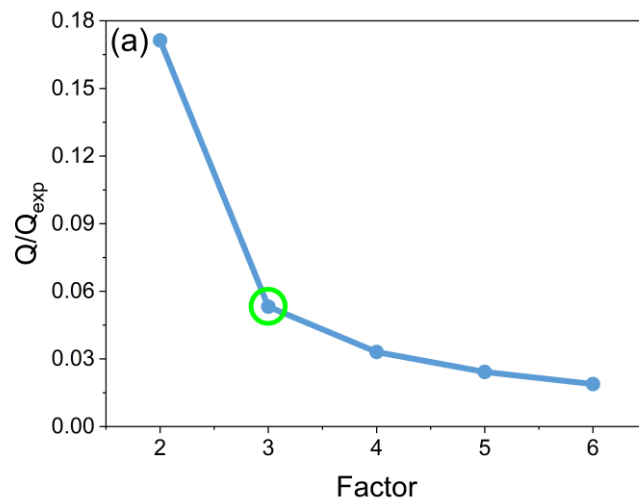
Figure S11. The $Q/Q_{expected}$ ratios of different factors resolved by PMF model at (a) East China sites (unimodal absorption spectral type) and (b) outside East China sites (bimodal absorption spectral type).
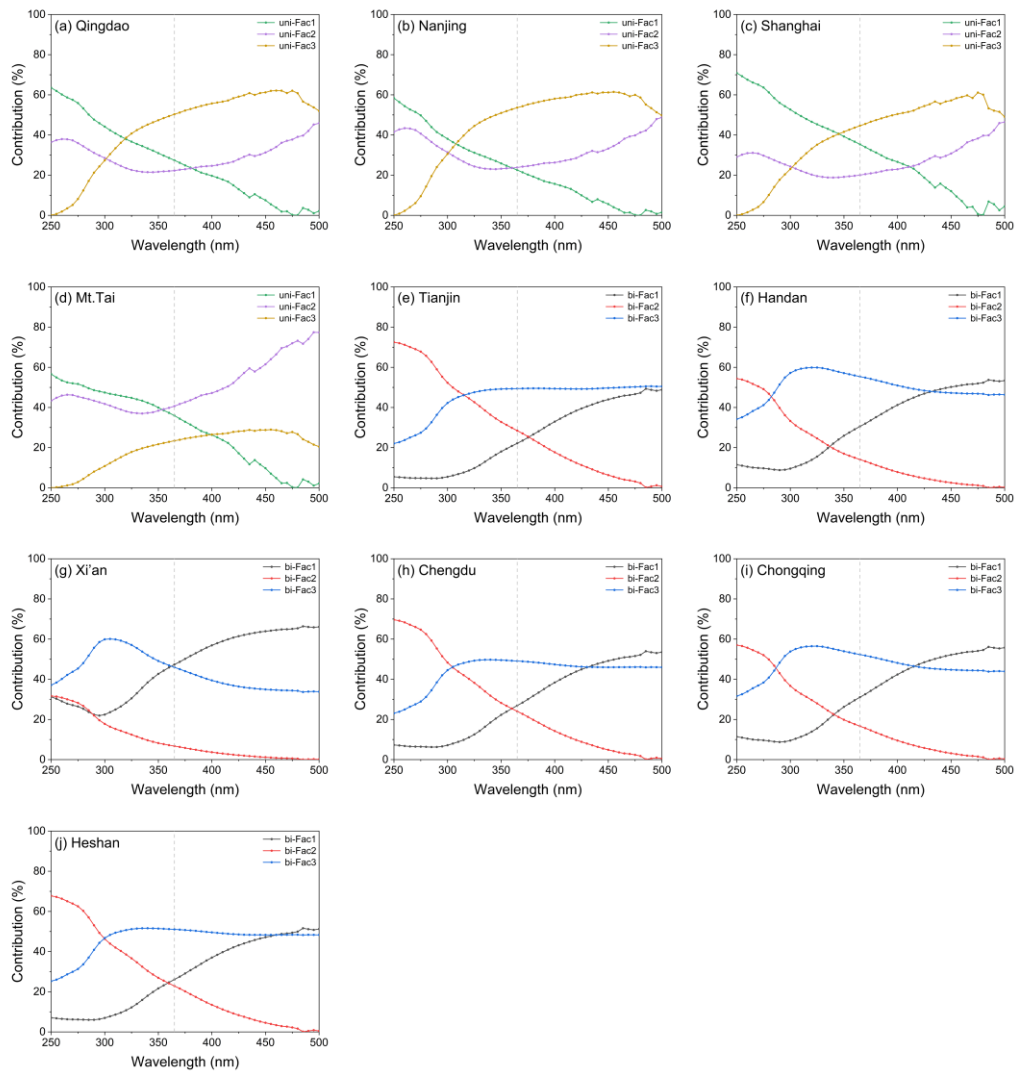
Figure S12. The proportional contributions of different factors at different wavelengths at (a-d) East China sites and (e-j) outside East China sites. Note: The dotted line represents the position of 365 nm.

165
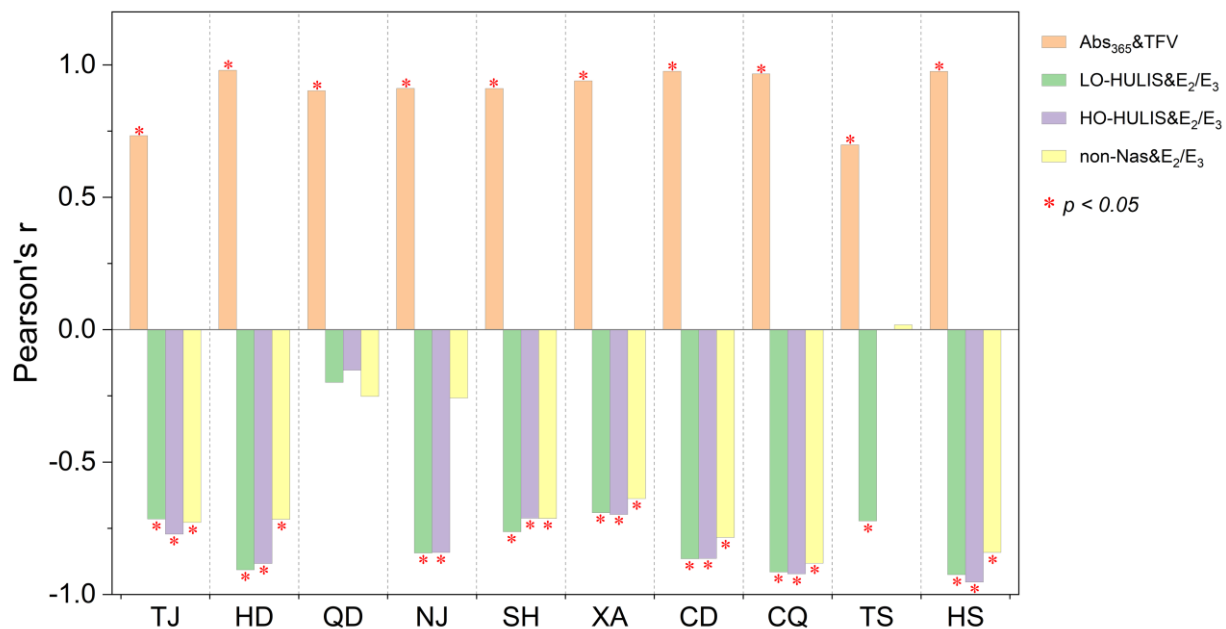
Figure S13. Pearson's correlation coefficients and significance levels (p, two-tailed) between Abs_{365} and TFV, E_2/E_3 and F_{max} of each fluorophore at each site.
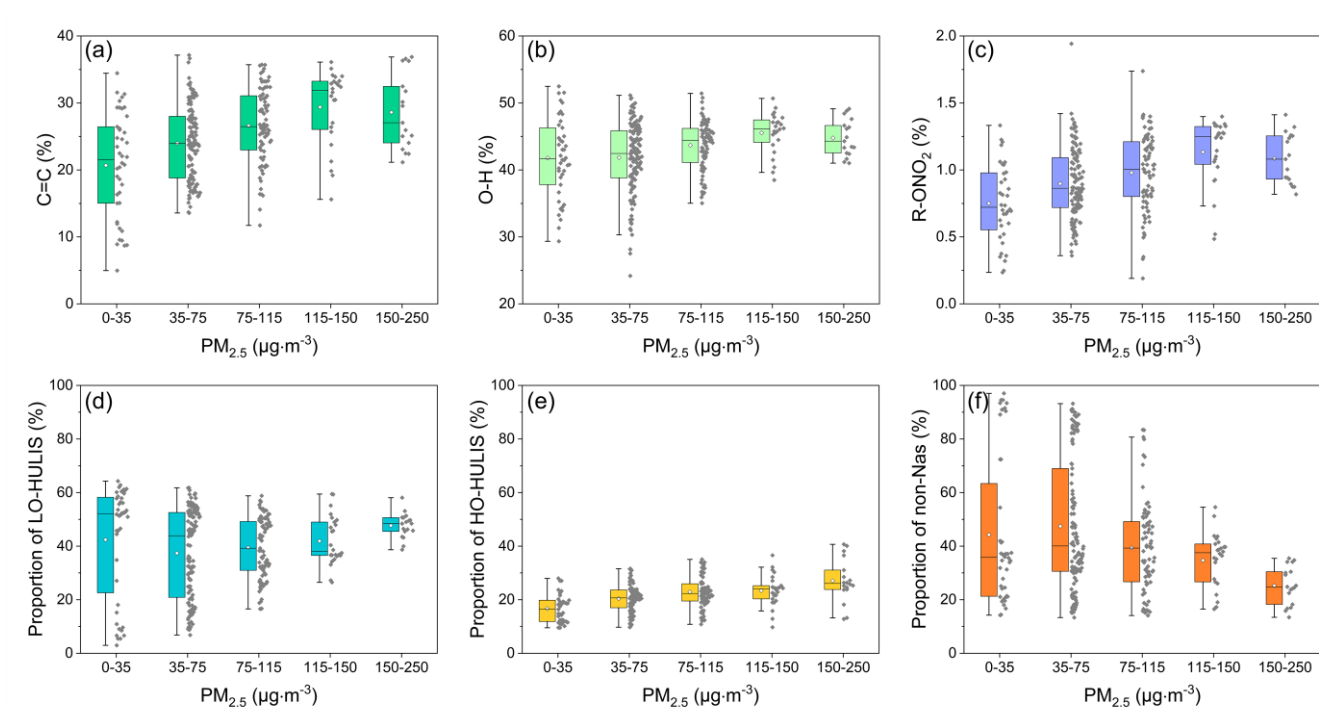
Figure S14. Variations of the relative abundance of functional groups (a) C=C, (b) O-H and (c) R-ONO$_2$ and the proportion of (d) LO-HULIS, (e) HO-HULIS and (f) non-Nas fluorophores with PM$_{2.5}$ mass concentrations.
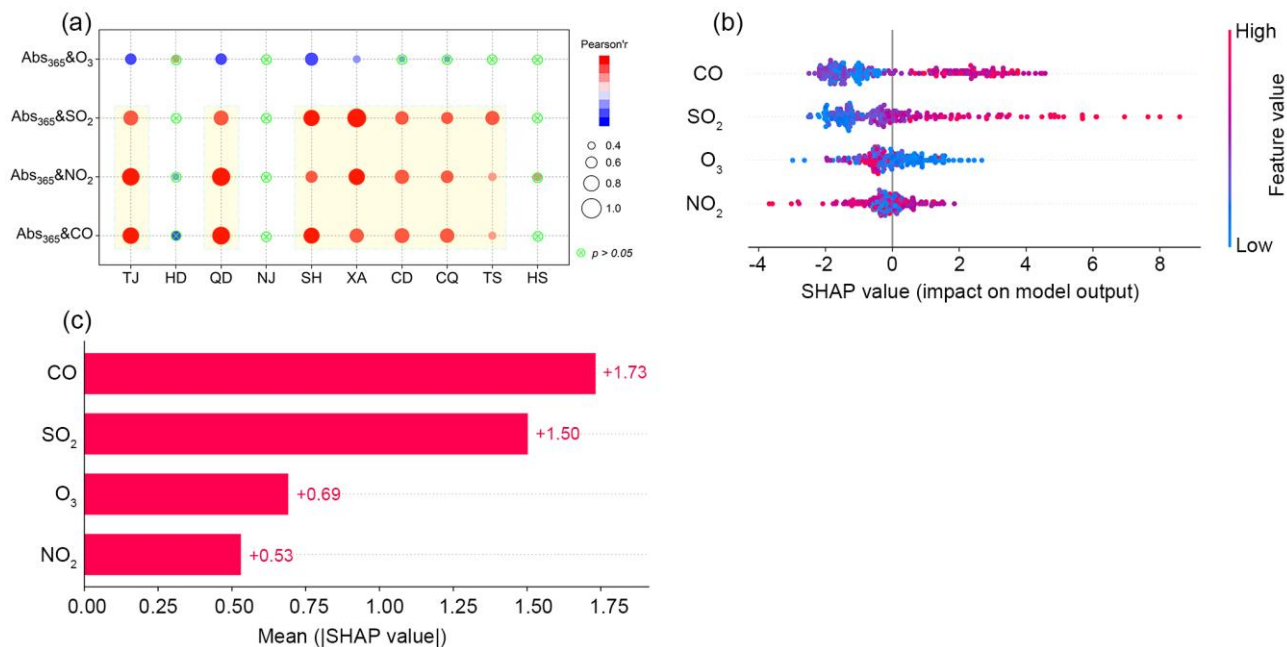
175 **Figure S15.** (a) Correlations between Abs_{365} and conventional air pollutants, and (b) SHAP summary plot (the color of the scatter plot from blue to red indicates an increase in factor values), and (c) schematic of chemical component ordering, with SHAP values indicating the contribution of each factor to Abs_{365}.
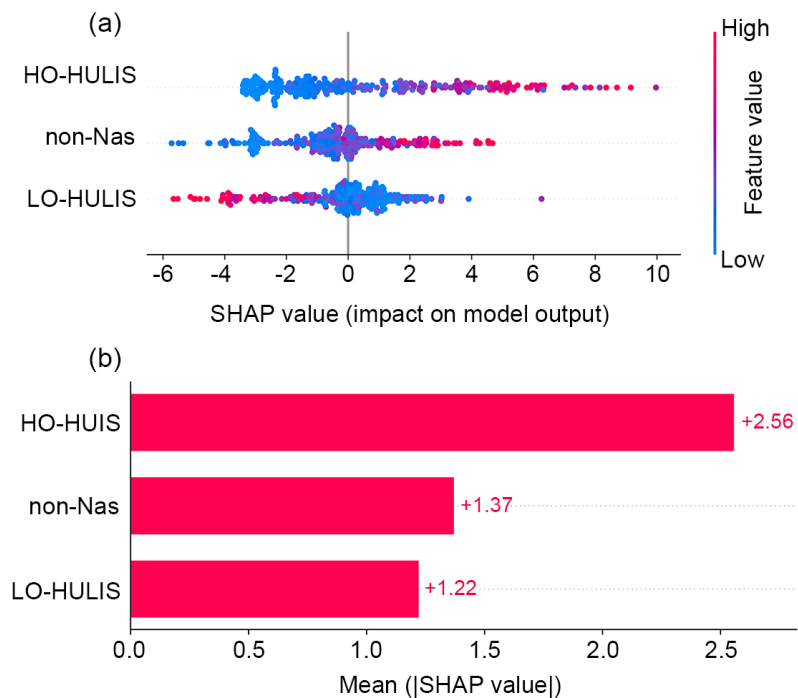
Figure S16. SHAP values calculated based on the XGBoost-SHAP model. (a) SHAP summary plot (the color of the scatter plot from blue to red indicates an increase in factor values), (b) schematic of chemical component ordering with SHAP values indicating the contribution of each factor to Abs_{365}.

References

Afsana, S., Zhou, R., Miyazaki, Y., Tachibana, E., Deshmukh, D. K., Kawamura, K., and Mochida, M.: Abundance, chemical structure, and light absorption properties of humic-like substances (HULIS) and other organic fractions of forest aerosols in
185   Hokkaido, Sci. Rep., 12, 14379, https://doi.org/10.1038/s41598-022-18201-z, 2022.

Bond, T. C. and Bergstrom, R. W.: Light absorption by carbonaceous particles: An investigative review, Aerosol Sci. Tech., 40, 27-67, https://doi.org/10.1080/02786820500421521, 2006.

Bro, R.: PARAFAC. Tutorial and applications, Chemometr. Intell. Lab. Syst., 38, 149-171, https://doi.org/10.1016/s0169-7439(97)00032-4, 1997.

190   Chen, Y. and Bond, T. C.: Light absorption by organic carbon from wood combustion, Atmos. Chem. Phys., 10, 1773-1787, https://doi.org/10.5194/acp-10-1773-2010, 2010.

Deng, J., Ma, H., Wang, X., Zhong, S., Zhang, Z., Zhu, J., Fan, Y., Hu, W., Wu, L., Li, X., Ren, L., Pavuluri, C. M., Pan, X., Sun, Y., Wang, Z., Kawamura, K., and Fu, P.: Measurement report: Optical properties and sources of water-soluble brown carbon in Tianjin, North China-insights from organic molecular compositions, Atmos. Chem. Phys., 22, 6449-6470,
195   https://doi.org/10.5194/acp-22-6449-2022, 2022.

Fan, X., Cheng, A., Chen, D., Cao, T., Ji, W., Song, J., and Peng, P.: Investigating the molecular weight distribution of atmospheric water-soluble brown carbon using high-performance size exclusion chromatography coupled with diode array and fluorescence detectors, Chemosphere, 338, 139517, https://doi.org/10.1016/j.chemosphere.2023.139517, 2023.

Gao, Y., Wang, Z., Li, Y., Luo, H., and Zhou, Z.: Aqueous brown carbon formation by aldehyde compounds reaction with
200   Glycine/Ammonium sulfate, Spectrochim. Acta A Mol. Biomol. Spectrosc., 248, 119230, https://doi.org/10.1016/j.saa.2020.119230, 2021.

He, W. and Hur, J.: Conservative behavior of fluorescence EEM-PARAFAC components in resin fractionation processes and its applicability for characterizing dissolved organic matter, Water Res., 83, 217-226, https://doi.org/10.1016/j.watres.2015.06.044, 2015.

205   Hecobian, A., Zhang, X., Zheng, M., Frank, N., Edgerton, E. S., and Weber, R. J.: Water-soluble organic aerosol material and the light-absorption characteristics of aqueous extracts measured over the Southeastern United States, Atmos. Chem. Phys., 10, 5965-5977, https://doi.org/10.5194/acp-10-5965-2010, 2010.

Lawaetz, A. J. and Stedmon, C. A.: Fluorescence intensity calibration using the Raman scatter peak of water, Appl. Spectrosc., 63, 936-940, https://doi.org/10.1366/000370209788964548, 2009.

210   Lee, H. J., Laskin, A., Laskin, J., and Nizkorodov, S. A.: Excitation-emission spectra and fluorescence quantum yields for fresh and aged biogenic secondary organic aerosols, Environ. Sci. Technol., 47, 5763-5770, https://doi.org/10.1021/es400644c, 2013.

Li, P., Yue, S., Yang, X., Liu, D., Zhang, Q., Hu, W., Hou, S., Zhao, W., Ren, H., Li, G., Gao, Y., Deng, J., Xie, Q., Sun, Y., Wang, Z., and Fu, P.: Fluorescence properties and chemical composition of fine particles in the background atmosphere of North China, Adv. Atmos. Sci., 40, 1159-1174, https://doi.org/10.1007/s00376-022-2208-x, 2023a.

215   Li, R., Zhang, M., Du, Y., Wang, G., Shang, C., Liu, Y., Zhang, M., Meng, Q., Cui, M., and Yan, C.: Impacts of dust events on

chemical characterization and associated source contributions of atmospheric particulate matter in northern China, Environ. Pollut., 316, 120597, https://doi.org/10.1016/j.envpol.2022.120597, 2023b.

Li, R., Yan, C., Meng, Q., Yue, Y., Jiang, W., Yang, L., Zhu, Y., Xue, L., Gao, S., Liu, W., Chen, T., and Meng, J.: Key toxic components and sources affecting oxidative potential of atmospheric particulate matter using interpretable machine learning: Insights from fog episodes, J. Hazard. Mater., 465, 133175, https://doi.org/10.1016/j.jhazmat.2023.133175, 2024.

Li, X., Yu, F., Song, Y., Zhang, C., Yan, F., Hu, Z., Lei, Y., Tripathee, L., Zhang, R., Guo, J., Wang, Y., Chen, Q., Liu, L., Cao, J., and Wang, Q.: Water-soluble brown carbon in $PM_{2.5}$ at two typical sites in Guanzhong Basin: Optical properties, sources, and implications, Atmos. Res., 281, 106499, https://doi.org/10.1016/j.atmosres.2022.106499, 2023c.

Liu, J., Bergin, M., Guo, H., King, L., Kotra, N., Edgerton, E., and Weber, R. J.: Size-resolved measurements of brown carbon in water and methanol extracts and estimates of their contribution to ambient fine-particle light absorption, Atmos. Chem. Phys., 13, 12389-12404, https://doi.org/10.5194/acp-13-12389-2013, 2013.

Murphy, K. R., Butler, K. D., Spencer, R. G. M., Stedmon, C. A., Boehme, J. R., and Aiken, G. R.: Measurement of dissolved organic matter fluorescence in aquatic environments: An interlaboratory comparison, Environ. Sci. Technol., 44, 9405-9412, https://doi.org/10.1021/es102362t, 2010.

Qin, J. J., Zhang, L. M., Zhou, X. M., Duan, J. C., Mu, S. T., Xiao, K., Hu, J. N., and Tan, J. H.: Fluorescence fingerprinting properties for exploring water-soluble organic compounds in $PM_{2.5}$ in an industrial city of northwest China, Atmos. Environ., 184, 203-211, https://doi.org/10.1016/j.atmosenv.2018.04.049, 2018.

Saleh, R.: From measurements to models: Toward accurate representation of brown carbon in climate calculations, Curr. Pollut. Rep., 6, 90-104, https://doi.org/10.1007/s40726-020-00139-3, 2020.

Stedmon, C. A. and Bro, R.: Characterizing dissolved organic matter fluorescence with parallel factor analysis: a tutorial, Limnol Oceanogr-Meth, 6, 572-579, https://doi.org/10.4319/lom.2008.6.572, 2008.

Ting, Y.-C., Ko, Y.-R., Huang, C.-H., Cheng, Y.-H., and Huang, C.-H.: Optical properties and potential sources of water-soluble and methanol-soluble organic aerosols in Taipei, Taiwan, Atmos. Environ., 290, 119364, https://doi.org/10.1016/j.atmosenv.2022.119364, 2022.

Wen, H., Zhou, Y., Xu, X., Wang, T., Chen, Q., Chen, Q., Li, W., Wang, Z., Huang, Z., Zhou, T., Shi, J., Bi, J., Ji, M., and Wang, X.: Water-soluble brown carbon in atmospheric aerosols along the transport pathway of Asian dust: Optical properties, chemical compositions, and potential sources, Sci. Total Environ., 789, 147971, https://doi.org/10.1016/j.scitotenv.2021.147971, 2021.

Wu, G., Fu, P., Ram, K., Song, J., Chen, Q., Kawamura, K., Wan, X., Kang, S., Wang, X., Laskin, A., and Cong, Z.: Fluorescence characteristics of water-soluble organic carbon in atmospheric aerosol, Environ. Pollut., 268, 115906, https://doi.org/10.1016/j.envpol.2020.115906, 2021.

Xie, X., Chen, Y., Nie, D., Liu, Y., Liu, Y., Lei, R., Zhao, X., Li, H., and Ge, X.: Light-absorbing and fluorescent properties of atmospheric brown carbon: A case study in Nanjing, China, Chemosphere, 251, 126350, https://doi.org/10.1016/j.chemosphere.2020.126350, 2020.

250 Yan, C. Q., Zheng, M., Sullivan, A. P., Bosch, C., Desyaterik, Y., Andersson, A., Li, X. Y., Guo, X. S., Zhou, T., Gustafsson, O., and Collett, J. L.: Chemical characteristics and light-absorbing property of water-soluble organic carbon in Beijing: Biomass burning contributions, Atmos. Environ., 121, 4-12, https://doi.org/10.1016/j.atmosenv.2015.05.005, 2015.

Yu, F., Li, X., Zhang, R., Guo, J., Yang, W., Tripathee, L., Liu, L., Wang, Y., Kang, S., and Cao, J.: Insights into dissolved organics in non-urban areas - Optical properties and sources, Environ. Pollut., 329, 121641,
255 https://doi.org/10.1016/j.envpol.2023.121641, 2023.

Zepp, R. G., Sheldon, W. M., and Moran, M. A.: Dissolved organic fluorophores in southeastern US coastal waters: correction method for eliminating Rayleigh and Raman scattering peaks in excitation-emission matrices, Mar. Chem., 89, 15-36, https://doi.org/10.1016/j.marchem.2004.02.006, 2004.

Zhan, Y., Tsona, N. T., Li, J., Chen, Q., and Du, L.: Water-soluble matter in $PM_{2.5}$ in a coastal city over China: Chemical
260 components, optical properties, and source analysis, J. Environ. Sci., 114, 21-36, https://doi.org/10.1016/j.jes.2021.07.011, 2022.

Zhang, C., Chen, M., Kang, S., Yan, F., Han, X., Gautam, S., Hu, Z., Zheng, H., Chen, P., Gao, S., Wang, P., and Li, C.: Light absorption and fluorescence characteristics of water-soluble organic compounds in carbonaceous particles at a typical remote site in the southeastern Himalayas and Tibetan Plateau, Environ. Pollut., 272, 116000,
265 https://doi.org/10.1016/j.envpol.2020.116000, 2021.

Zhong, M., Xu, J., Wang, H., Gao, L., Zhu, H., Zhai, L., Zhang, X., and Zhao, W.: Characterizing water-soluble brown carbon in fine particles in four typical cities in northwestern China during wintertime: integrating optical properties with chemical processes, Atmos. Chem. Phys., 23, 12609-12630, https://doi.org/10.5194/acp-23-12609-2023, 2023.